International Journal of Nanomedicine

Dovepress
open access to scientific and medical research

Open Access Full Text Article

ORIGINAL RESEARCH

Photothermal exposure of polydopamine-coated branched Au–Ag nanoparticles induces cell cycle arrest, apoptosis, and autophagy in human bladder cancer cells

This article was published in the following Dove Press journal:
International Journal of Nanomedicine

Xiaoming Zhao[1,*]
Tianyang Qi[1,*]
Chenfei Kong[1]
Miao Hao[1]
Yuqian Wang[1]
Jing Li[1]
Baocai Liu[2]
Yiyao Gao[1]
Jinlan Jiang[1]

[1]Scientific Research Center, China-Japan Union Hospital of Jilin University, Changchun, China; [2]Department of Radiation Oncology, China-Japan Union Hospital of Jilin University, Changchun, China

*These authors contributed equally to this work

Purpose: Polydopamine-coated branched Au–Ag nanoparticles (Au–Ag@PDA NPs) exhibit good structural stability, biocompatibility, and photothermal performance, along with potential anticancer efficacy. Here, we investigated the cytotoxicity of Au–Ag@PDA NPs against human bladder cancer cells (T24 cells) in vitro and in vivo, as well as the underlying molecular mechanisms of photothermal therapy-induced T24 cell death.

Materials and methods: T24 cells were treated with different doses of Au–Ag@PDA NPs followed by 808 nm laser irradiation, and the effects on cell proliferation, cell cycle, apoptosis, and autophagy were analyzed. To confirm the mechanisms of inhibition, real-time PCR and Western blot analysis were used to evaluate markers of cell cycle, apoptosis, autophagy, and the AKT/ERK signaling pathway. Moreover, we evaluated the effects of the treatment on mitochondrial membrane potential and ROS generation to confirm the underlying mechanisms of inhibition. Finally, we tested the T24 tumor inhibitory effects of Au–Ag@PDA NPs plus laser irradiation in vivo using a xenograft mouse model.

Results: Au–Ag@PDA NPs, with appropriate laser irradiation, dramatically inhibited the proliferation of T24 cells, altered the cell cycle distribution by increasing the proportion of cells in the S phase, induced cell apoptosis by activating the mitochondria-mediated intrinsic pathway, and triggered a robust autophagy response in T24 cells. Moreover, Au–Ag@PDA NPs decreased the expression of phosphorylated AKT and ERK and promoted the production of ROS that function upstream of apoptosis and autophagy. In addition, Au–Ag@PDA NP-mediated photothermolysis also significantly suppressed tumor growth in vivo.

Conclusion: This preclinical study can provide a mechanistic basis for Au–Ag@PDA NP-mediated photothermal therapy toward promotion of this method in the clinical treatment of bladder cancer.

Keywords: nanoparticles, photothermal therapy, near-infrared laser, cell cycle, apoptosis, autophagy

Introduction

Cancer remains a major threat to human health worldwide with high mortality rates. Thus, the development of strategies to completely cure cancer is a great challenge. In recent years, photothermal therapy has attracted increasing attention as the fifth-line tumor treatment after surgery, chemotherapy, radiotherapy, and biological therapy.[1,2] This treatment involves the selective accumulation of nanomaterials with near-infrared (NIR) photothermal conversion at the tumor site, which then absorb the NIR light and

Correspondence: Jinlan Jiang
Scientific Research Center, China-Japan Union Hospital of Jilin University, 126 Xiantai Street, Changchun, Jilin 130033, China
Tel +86 43 18 499 5382
Email jiangjinlan@jlu.edu.cn

submit your manuscript | www.dovepress.com
Dovepress
http://dx.doi.org/10.2147/IJN.S174349

are efficiently converted into heat energy to easily kill tumor cells while minimizing the damage to normal tissues and organs.[3–5] The most important advantage of photothermal therapy is that it can theoretically achieve effective treatment for all solid tumors, including those that have failed to respond to radiotherapy and chemotherapy along with drug-resistant tumors, without producing the cytotoxicity associated with conventional radiotherapy and chemotherapy that decreases the quality of life of patients.[6–8]

Research on photothermal therapy is currently focused on the development of nanomaterials with high photothermal conversion efficiencies. Precious metal nanomaterials such as gold nanoparticles (Au NPs) with surface plasmon resonance are considered to be ideal photothermal conversion materials, resulting in enhanced optical absorption that is directly related to the photothermal effects.[9–11] Au NPs can be easily prepared by controlling the effective size and aspect ratio, which strongly determine their properties such as photothermal conversion and biocompatibility.[12–14] Compared with several conventional spherical smooth nanostructures such as rods, wires, shells, cages, and stars, branched Au NPs have emerged as novel Au nanostructures with many advantages, including highly branched structures and a large specific surface area, resulting in an even higher photothermal transduction efficiency.[15–17] However, branched Au NPs possess less structural stability and it is more difficult to adjust the plasmon resonance absorption peak at 808 nm, which has thus far limited their applicability in tumor treatment. In order to further improve the structural stability, biocompatibility, and photothermal conversion efficiency, methods of coating the Au NPs with shells have attracted substantial attention. For example, Au@Pt with nanostructured dendritic Pt shells has been successfully synthesized.[18–22] Recently, Li et al[23] proposed that branched Au–Ag NPs coated with polydopamine (PDA) would exhibit excellent structural stability, biocompatibility, and photothermal properties. The photothermal property of branched Au NPs is enhanced by the Au–Ag nanostructures, while the PDA coating strongly improves the structural stability and biocompatibility. More importantly, these NPs could effectively suppress the growth of HeLa cells after laser irradiation.[23] However, no detailed data are available concerning the potential mechanisms involved in the process by which Au–Ag@PDA NPs inhibit cancer cell proliferation.

Therefore, in the present study, we analyzed the inhibitory mechanisms of Au–Ag@PDA NPs with respect to cancer cell proliferation, including analysis of the cell cycle, apoptosis, mitochondrial membrane potential, and autophagy, in a human bladder cancer cell line (T24 cells) in vitro. Given the established roles of the AKT/ERK signaling pathway and ROS as some of the early changes linked to apoptosis and autophagy, we further examined their potential involvement in the inhibitory effects induced by Au–Ag@PDA NPs. Moreover, we explored the antitumor effect of Au–Ag@PDA NPs in vivo using a T24 xenograft mouse model. This work highlights the great potential application of Au–Ag@PDA NPs in the treatment of bladder cancer.

Materials and methods

Preparation and characterization of Au–Ag@PDA NPs

Au–Ag@PDA NPs were kindly provided by Dr Zhang Hao (Jilin University, Changchun, China) and prepared as previously described, and are shown in Figure 1A.[23] First, Ag seeds were synthesized according to the citrate reduction approach. Second, branched Au–Ag NPs were prepared using sacrificial Ag seeds, $HAuCl_4$ aqueous solution, and the reductant of hydroquinone under room temperature. Third, to synthesize Au–Ag@PDA NPs, Tris buffer was added into the as-prepared Au–Ag NPs solution to alter the solution pH to 8.5, followed by addition of a dopamine solution and incubation at room temperature for 3 hours. Finally, Au–Ag@PDA NPs were obtained by centrifugation and washing with deionized water. According to the method reported by Roper et al[24] and Tian et al,[25] the photothermal transduction efficiency (η) of Au–Ag@PDA NPs with a PDA thickness of 15 nm reached up to 61.4% at 808 nm.[23] Ultraviolet–visible absorption spectra were determined using a UV-2550 spectrophotometer (Shimadzu, Kyoto, Japan) at room temperature (28°C). Transmission electron microscopy (TEM) images were obtained using a Hitachi H-800 electron microscope at an acceleration voltage of 200 kV with a charge-coupled device camera.

Cell culture

The human bladder cancer cell line T24 and the human cervix epithelial carcinoma cell line HeLa were obtained from American Type Culture Collection (ATCC; Manassas, VA, USA). The cells were cultured in DMEM with high glucose, 10% FBS, 100 units/mL penicillin, and 100 μg/mL streptomycin in a 5% CO_2 incubator at 37°C. The cells were digested with 0.25% trypsin/EDTA when reaching nearly 80% confluence.

Transmission electron microscopy

TEM analysis was used to observe the intracellular localization of the Au–Ag@PDA NPs. The cells were incubated

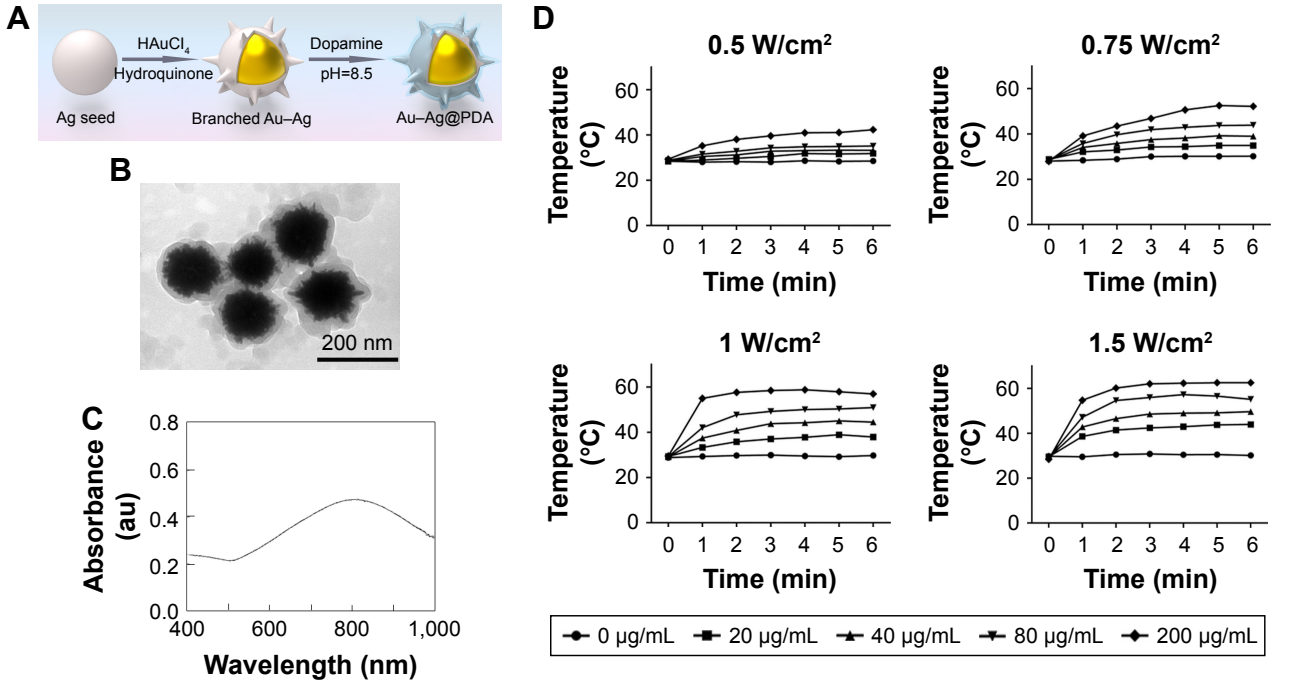

Figure 1 Characterization of Au–Ag@PDA NPs.
Notes: (**A**) Schematic diagram of Au–Ag@PDA NPs synthesis. (**B**) TEM images of Au–Ag@PDA NPs. (**C**) UV-vis spectra of Au–Ag@PDA NPs. (**D**) Temperature increase of different concentrations of Au–Ag@PDA NPs irradiated by an 808 nm laser at various power densities.
Abbreviations: NPs, nanoparticles; PDA, polydopamine; TEM, transmission electron microscopy; UV, ultraviolet.

with Au–Ag@PDA NPs (20 μg/mL) for 24 hours, and then collected and fixed in 4% glutaraldehyde for 2 hours. The ultrastructural features were observed using Tecnai Spirit TEM (FEI Company, Hillsboro, OR, USA).

Cell viability

Cell Counting Kit-8 (CCK-8; Dojindo, Kyushu, Japan) assays were used to assess the potential cytotoxicity of Au–Ag@PDA NPs. T24 cells were seeded in 96-well plates at a density of 5×10^3 cells/well. After culturing overnight, different concentrations of Au–Ag@PDA NPs were added to the 96-well plates and the cells were subsequently cultured for 24 hours. The cells were exposed to an 808 nm laser (Shanghai Connet Fiber Optics Company, Shanghai, China) at a power density of 1 W/cm^2 for 4 minutes and then incubated for another 24 hours. Subsequently, 10 μL of CCK-8 reagent was added to each well and the cells were further cultured for 3 hours. The absorbance at 450 nm was determined using a microplate reader (Synergy HT; BioTek Instruments, Winooski, VT, USA) and the cell viability was calculated as: (OD test sample/OD control cells)×100%.

Propidium iodide (PI; Beyotime Biotech, Nantong, China) and Hoechst 33342 (Beyotime Biotech) staining was also performed to quantify the necrotic cells. After laser irradiation, the cells were washed twice with PBS and stained with PI and Hoechst 33342 at 37°C for 20 minutes in the dark. The cells were washed with PBS and then observed with High-Content Imaging System (Perkin-Elmer Operetta®, Waltham, MA, USA) to count the stained cells.

Cell cycle

The distribution of DNA in different stages of the cell cycle was determined by flow cytometry (FCM). Approximately 5×10^4 cells/well were seeded in six-well cell culture plates. The cells were exposed to different concentrations of Au–Ag@PDA NPs (20–40 μg/mL) for 24 hours, followed by irradiation with 808 nm NIR laser at 1 W/cm^2 for 4 minutes. After irradiation, the cells were further cultured for 3 and 24 hours, respectively, harvested, and fixed in ice-cold 70% ethanol overnight at 4°C. Prior to FCM analysis, the cell solutions were centrifuged and resuspended in 0.5 mL of a cold PBS solution containing 0.01% RNase A and 0.5% PI. The cells were then incubated at 4°C until FCM analysis (FC500; Beckman Coulter Inc., Fullerton, CA, USA).

Cell apoptosis

Apoptosis was analyzed using two methods: FCM and Hoechst 33342 staining. In FCM, the cells were collected by trypsinization, washed three times with ice-cold PBS solution, and stained with 500 μL binding buffer containing

5 μL Annexin V-fluorescein isothiocyanate (Beyotime Biotech) and 5 μL PI at room temperature for 15 minutes in the dark; the stained cells were then analyzed by FCM (FC500; Beckman Coulter Inc.). The signals of early and late apoptotic cells were located in the lower and upper right quadrant of the resulting dot plot, respectively. In Hoechst 33342 staining, the cells were washed twice with PBS and stained with Hoechst 33342 (Beyotime Biotech) at 37°C for 20 minutes in the dark. The cells were then washed with PBS and cell nuclei were visualized under the High-Content Imaging System (Perkin-Elmer Operetta).

RNA isolation and real-time PCR

Total RNA was isolated with Tripure Isolation reagent (Roche Applied Science, Mannheim, Germany) according to the manufacturer's protocol. RNA was subjected to reverse transcription using Transcriptor First Strand cDNA Synthesis Kit (Roche Applied Science) following the manufacturer's instructions. Real-time quantitative PCR was performed with the SYBR Green PCR kit from Roche Applied Science. Reactions were cycled between 95°C for 15 seconds and 60°C for 30 seconds for 40 cycles after a denaturation step at 95°C for 10 minutes. The detected mRNA expression levels were normalized by that of β-actin. The primer pairs were as follows: BCL2, 5′-CTGCACCTGACGCCCTTCACC-3′ (forward) and 5′-CACATGACCCCACCGAACTCAAAGA-3′ (reverse); BCLX, 5′-GATCCCCATGGCAGCAGTAAAGCAAG-3′ (forward) and 5′-CCCCATCCCGGAAGAGTTCATTCACT-3′ (reverse); β-actin, 5′-ATGGGTCAGAAGGATTCCTATGT-3′ (forward) and 5′-AGCCACACGCAGCTCATT-3′ (reverse).

Western blot analysis

After irradiation (808 nm, 1 W/cm^2, 4 minutes), the cells were further cultured for 3 and 24 hours, respectively, and the cell pellet was lysed in RIPA buffer for 30 minutes on ice. The proteins from each sample were then separated by 8%–15% SDS-PAGE. After transferring onto polyvinylidene difluoride membranes, the membranes were incubated with 5% (w/v) non-fat milk in Tris-buffered saline-Tween buffer and then with the primary antibody at 4°C overnight, followed by incubation with the secondary antibody goat anti-rabbit IRDye 800 (Li-Cor Biosciences, Lincoln, NE, USA) at room temperature for 30 minutes. Primary antibodies against p21 (2947), caspase 3 (14220), caspase 8 (4790), ERK (4695), p-ERK (4370), AKT (4691), p-AKT (Ser473) (4060), and cytochrome *c* (4272) were purchased from Cell Signaling Technology (Danvers, MA, USA). The antibodies against cyclin A (18202-1-AP), BAX (23931-1-AP), and GAPDH (10494-1-AP) were obtained from Proteintech (Wuhan, China). The antibody against LC3 (L7543) was obtained from Sigma-Aldrich (St Louis, MO, USA). The bound images were acquired using the Odyssey Infrared Imaging System (Li-Cor Biosciences).

Mitochondrial membrane potential ($\Delta\Psi$m) measurement

The mitochondrial membrane potential ($\Delta\Psi$m) was estimated using a JC-1 kit (Beyotime Biotech) according to the manufacturer's protocol. In brief, the cells were trypsinized, incubated with JC-1 solution at 37°C for 20 minutes, washed twice with PBS, and then analyzed using FCM (FACSCanto II; Becton, Dickinson and Company, Franklin Lakes, NJ, USA). Green and red fluorescence was analyzed to distinguish between cells with intact mitochondria (high membrane potential) and those undergoing apoptosis (lower membrane potential) using the appropriate gates.

Cytosolic isolation

Cytosolic fractions were obtained according to the instructions of the cell mitochondria isolation kit (Beyotime Biotech).

Intracellular ROS measurement

The level of ROS generation was estimated using dichloro-dihydrofluorescein diacetate fluorescent dye (Beyotime Biotech). The cells were harvested using 0.25% trypsin/EDTA and then centrifuged at 135× *g* for 5 minutes. The supernatant was discarded and the pellet was resuspended in 1 mL PBS containing dichloro-dihydrofluorescein diacetate (20 μM), followed by incubation for 30 minutes at 37°C in the dark. The level of intracellular ROS was determined by FCM (FC500; Beckman Coulter Inc.). ROS generation was also monitored at 520 nm at the single-cell level using the High-Content Imaging System (Perkin-Elmer Operetta®).

Xenograft mouse tumor model

BALB/C nude mice (aged 6–8 weeks) were purchased from Beijing HFK Bioscience Co., Ltd (Beijing, China) and housed with sterile water and food. The treatment of animals and all animal experiments were approved by the Animal Welfare and Research Ethics Committee of Jilin University. The animal experiments were carried out following the internationally accepted animal care guidelines (EEC Directive of 1986; 86/609/EEC). The mice received subcutaneous injection of T24 tumor cells at a dose of 1×10^7/mL.

When the tumor size reached 50 mm^3, the nude mice were randomly divided into three groups (n=3 per group): control group (0.9% NaCl), Au–Ag@PDA NPs (50 μg) group, and Au–Ag@PDA NPs (100 μg) group. Mice of each group were intratumorally injected with 50 μL of 0.9% NaCl, 25 μL of 2 mg/mL Au–Ag@PDA NPs, or 50 μL of 2 mg/mL Au–Ag@PDA NPs. At 3 hours after subcutaneous injection, in vivo tumors were irradiated at 1 W/cm^2 for 4 minutes. The tumor size was measured using a Vernier caliper every 2–3 days after laser irradiation. The weight of each mouse was also measured at each time point. After 12 days, the mice were sacrificed, and the tumor tissues and other major organs were harvested and fixed in 5% formalin for H&E staining and TUNEL assays.

Histological analysis and TUNEL assays

The tumor tissues and major organs, including the heart, liver, spleen, lung, and kidney, were fixed with 5% formalin and embedded in paraffin blocks. Some paraffin sections were further stained with H&E according to the standard protocol, whereas others were subjected to TUNEL (Roche Applied Science) assays. Images of sections were observed using a fluorescence microscope (BX51T-PHD-J11; Olympus Corporation, Tokyo, Japan).

Statistical analysis

Data are expressed as the mean±SD of three independent experiments. Differences between groups were tested by one-way ANOVA. A P-value <0.05 was considered to be statistically significant.

Results

Characterization of Au–Ag@PDA NPs

A schematic illustration of the synthesis of Au–Ag@PDA NPs, based on the previously reported method,[23] is shown in Figure 1A. TEM images of the as-prepared Au–Ag@PDA NPs indicated that the dopamine formed a polymer shell on the branched Au–Ag NPs (Figure 1B). The particle size was uniform, and the mean grain size was ~200 nm. The ultraviolet–visible absorption spectra showed that the Au–Ag@PDA NPs generated an obvious longitudinal plasmon peak at 808 nm, which is the most commonly employed NIR wavelength in photothermal therapy (Figure 1C). Thus, we irradiated the Au–Ag@PDA NPs with an 808 nm NIR laser at various power densities (0.5–1.5 W/cm^2). During continuous irradiation, the temperature of the solutions rapidly rose initially along with the increase in Au–Ag@PDA NPs concentration and irradiation power, and then became stable (Figure 1D). At room temperature (28°C), irradiation with the 808 nm NIR laser at 1 W/cm^2 for 4 minutes caused the temperature of the solution containing 40 μg/mL Au–Ag@PDA NPs to rise, which stabilized at 46°C, in line with the requirements of the photothermal killing of tumor cells. By contrast, no noticeable temperature changes were observed in the blank medium without Au–Ag@PDA NPs because of the minimal absorption by the solution.

Cytotoxicity of Au–Ag@PDA NPs

TEM visualization was used to explore the ultrastructural features and cellular uptake of Au–Ag@PDA NPs. As shown in Figure 2A, Au–Ag@PDA NPs retained their original structure without aggregation after entering the cell, suggesting excellent stability and dispersion. In addition, the Au–Ag@PDA NPs appeared to have been internalized into the T24 cells by an endocytosis process, localizing mostly in the lysosomes, and apparently did not enter the cell nucleus (Figure 2A).

The CCK-8 results revealed that Au–Ag@PDA NPs alone had no apparent cytotoxicity on T24 cells up to a concentration of 200 μg/mL (Figure 2B). However, after laser irradiation at 1 W/cm^2 for 4 minutes, Au–Ag@PDA NPs caused T24 cell growth inhibition in the presence of 40 μg/mL Au–Ag@PDA NPs, and the inhibitory effect was enhanced with the increase of concentration. The control experiment showed that laser irradiation in the absence of Au–Ag@PDA NPs had no effect on the viability of T24 cells (Figure 2C). Similar results were detected with PI staining. Compared with the no-laser control group, laser irradiation alone led to no cell damage, given no visible red fluorescence indicating that all the cells had survived. However, with an increase of the concentration of Au–Ag@PDA NPs, several red dots appeared after 4 minutes of laser exposure, indicating that Au–Ag@PDA NPs followed by the laser irradiation led to the necrosis of cancer cells (Figure 2D). In general, these results suggest that Au–Ag@PDA NPs exhibit low cytotoxicity and good photothermal performance.

Effects of Au–Ag@PDA NPs on the cell cycle

Cell cycle progression was evaluated by FCM to determine the potential mechanism for the observed growth inhibition of T24 cells by Au–Ag@PDA NPs. In the absence of NPs, the laser irradiation had no effect on the cell cycle distribution of T24 cells. Interestingly, after laser treatment, Au–Ag@PDA NPs induced an increased proportion of cells in the S phase in a time- and dose-dependent manner (Figure 3A and B).

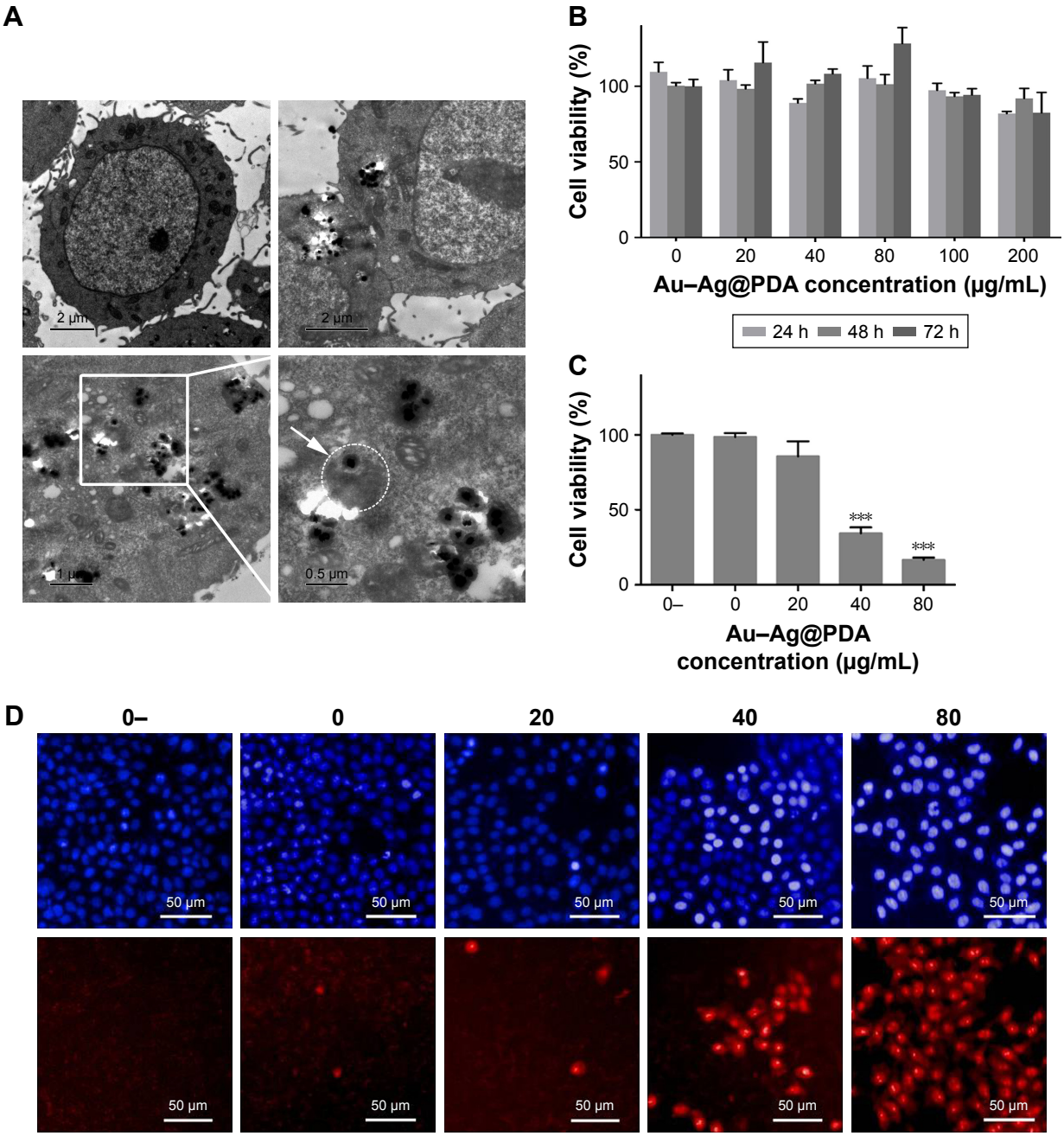

Figure 2 Cytotoxicity of Au–Ag@PDA NPs in T24 cells.

Notes: (**A**) Ultrastructural changes of T24 cells treated with Au–Ag@PDA NPs for 24 hours. Top left: control T24 cells. Top right: Au–Ag@PDA NPs were internalized into T24 cells via endocytic pathways. Bottom left and right: Au–Ag@PDA NPs deposited in the lysosome. White spots representing Au–Ag@PDA NPs were observed in the lysosome. (**B**) Cytotoxicity of Au–Ag@PDA NPs in T24 cells. (**C**) Cytotoxicity of Au–Ag@PDA NPs after 808 nm laser irradiation at 1 W/cm^2 for 4 minutes in T24 cells (0–: 0 μg+no laser, 0: 0 μg+laser, 20: 20 μg+laser, 40: 40 μg+laser, 80: 80 μg+laser). (**D**) Images of T24 cells treated with different concentrations of Au–Ag@PDA NPs after laser irradiation at 1 W/cm^2 for 4 minutes. Necrotic T24 cells were strongly stained by PI (red); cell nuclei were labeled by Hoechst 33342 (blue). Each experiment was performed three times. ***$P<0.001$ vs 0 group.

Abbreviations: NPs, nanoparticles; PDA, polydopamine; PI, propidium iodide.

To elucidate the mechanism underlying this effect, the expression levels of cyclin A and p21, related to S phase arrest, were determined by Western blot. As shown in Figure 3C and D, Au–Ag@PDA NPs plus laser exposure decreased the protein levels of cyclin A, but increased the protein levels of p21 in T24 cells in a time- and dose-dependent manner.

Effects of Au–Ag@PDA NPs on apoptosis

To determine whether the growth inhibition of T24 cells mediated by Au–Ag@PDA NPs was associated with apoptosis, FCM analysis and Hoechst 33342 staining were used. FCM showed a dramatic increase of cells in both early and late apoptosis in the presence of Au–Ag@PDA NPs

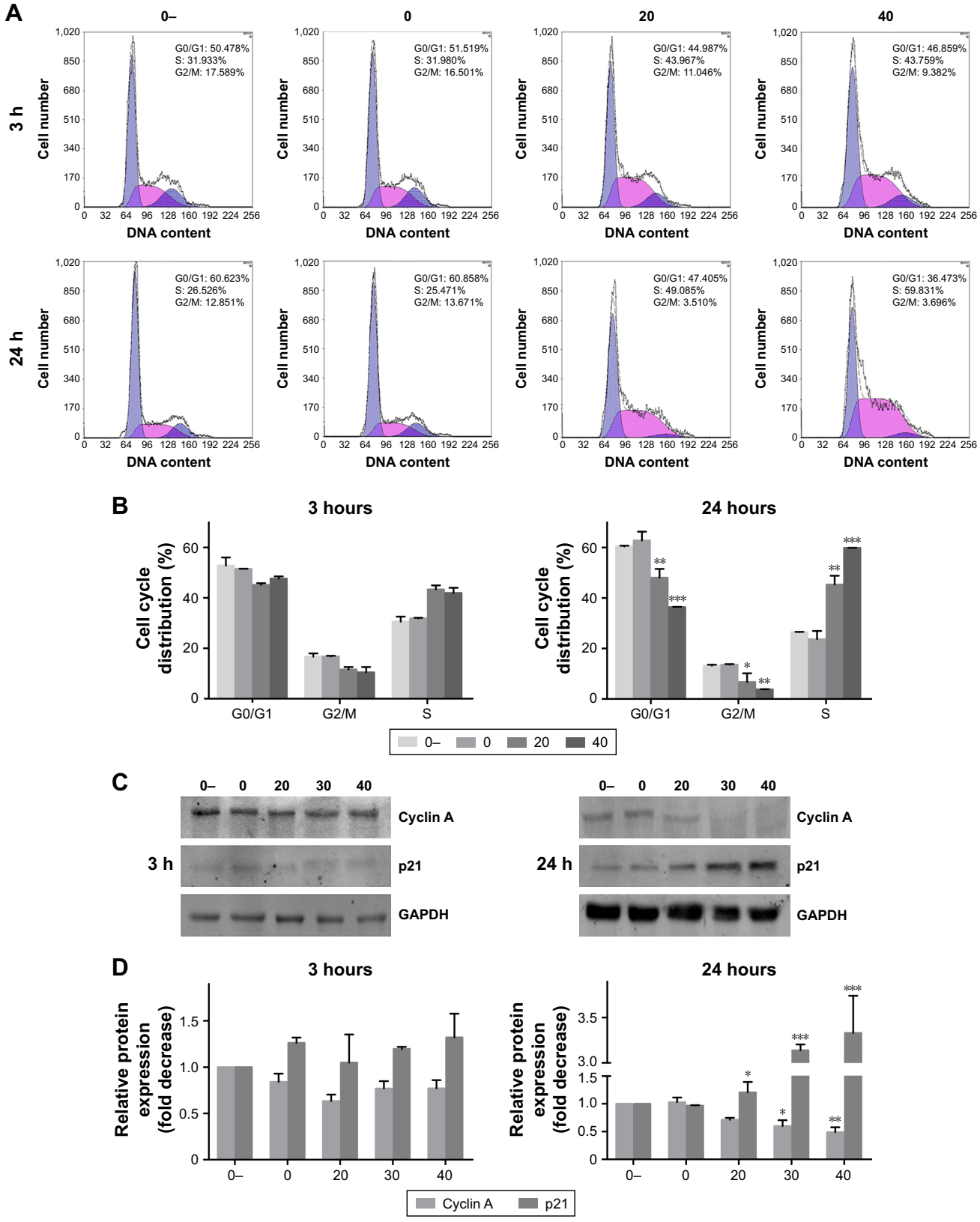

Figure 3 Au–Ag@PDA NPs induced S phase arrest and modulated key cell cycle regulators. The T24 cells were treated with different concentrations of Au–Ag@PDA NPs at 3 and 24 hours after laser irradiation with 1 W/cm^2 for 4 minutes (0–: 0 μg+no laser, 0: 0 μg+laser, 20: 20 μg+laser, 30: 30 μg+laser, 40: 40 μg+laser).

Notes: (**A**) Cell cycle distribution determined by FCM. (**B**) Time- and dose-dependent cell cycle arresting effect of Au–Ag@PDA NPs. (**C**) Expression levels of cell cycle-regulating proteins detected by Western blot. GAPDH was used to normalize protein levels. (**D**) Quantification of cyclin A and p21 protein levels compared with the 0– control group (mean±SD; n=3). *$P<0.05$, **$P<0.01$, ***$P<0.001$ vs 0 group.

Abbreviations: FCM, flow cytometry; NPs, nanoparticles; PDA, polydopamine.

followed by 808 nm NIR laser irradiation in a time- and dose-dependent manner (Figure 4A and B). Hoechst 33342 staining also showed obvious morphological characteristics of apoptosis in T24 cells incubated with Au–Ag@PDA NPs at 3 and 24 hours after laser irradiation. In particular, the apoptotic cells stained with Hoechst 33342 presented brighter blue fluorescence due to karyopyknosis and chromatin condensation in the Au–Ag@PDA NPs group compared with the control group. The ratio of dyed cells also increased with the increase in dosage of Au–Ag@PDA NPs (Figure 4C).

In addition, we investigated the changes of apoptosis-related gene expression the treatment of Au–Ag@PDA NPs plus laser irradiation. As shown in Figure 4D, E and F,

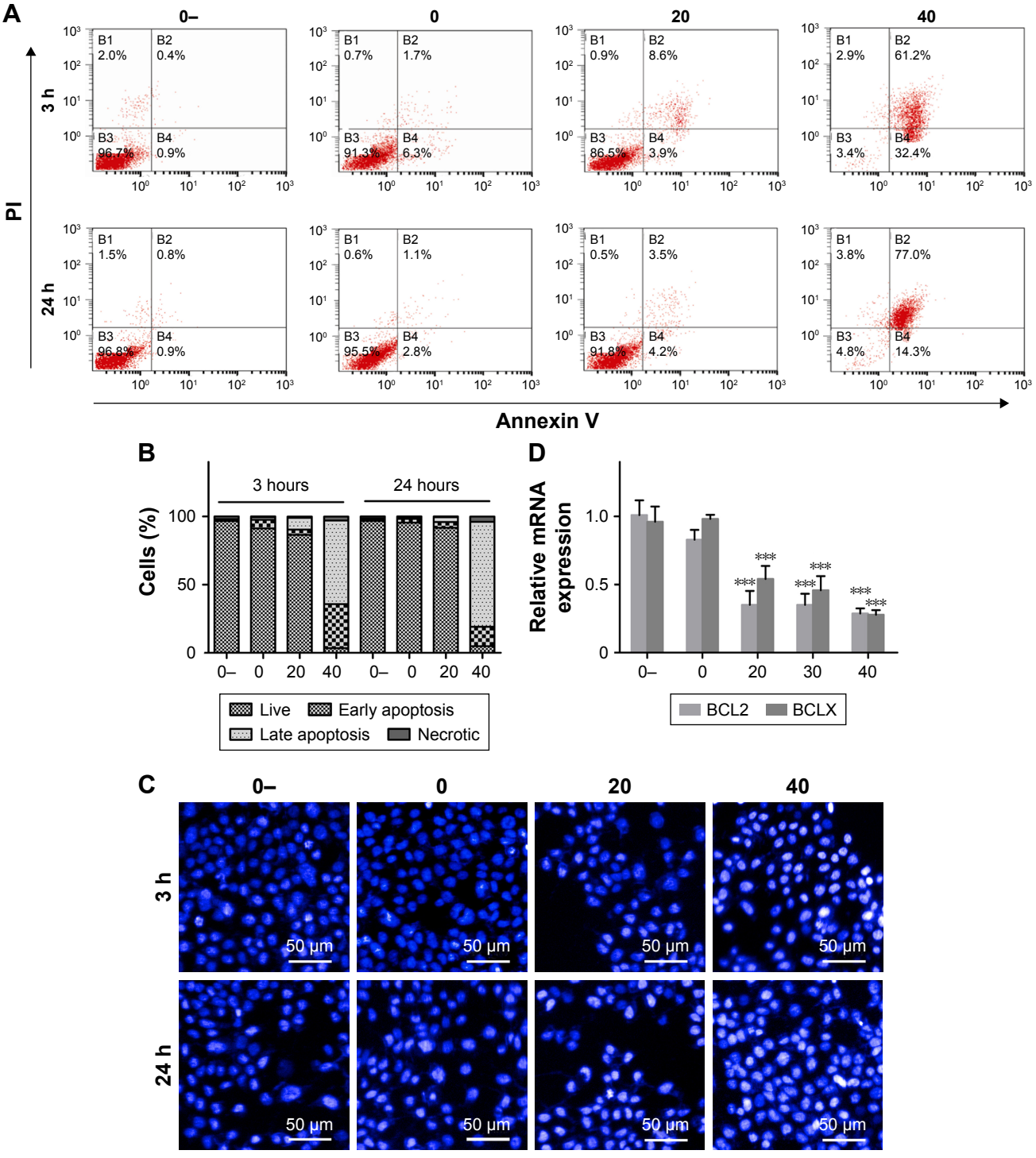

Figure 4 (*Continued*)

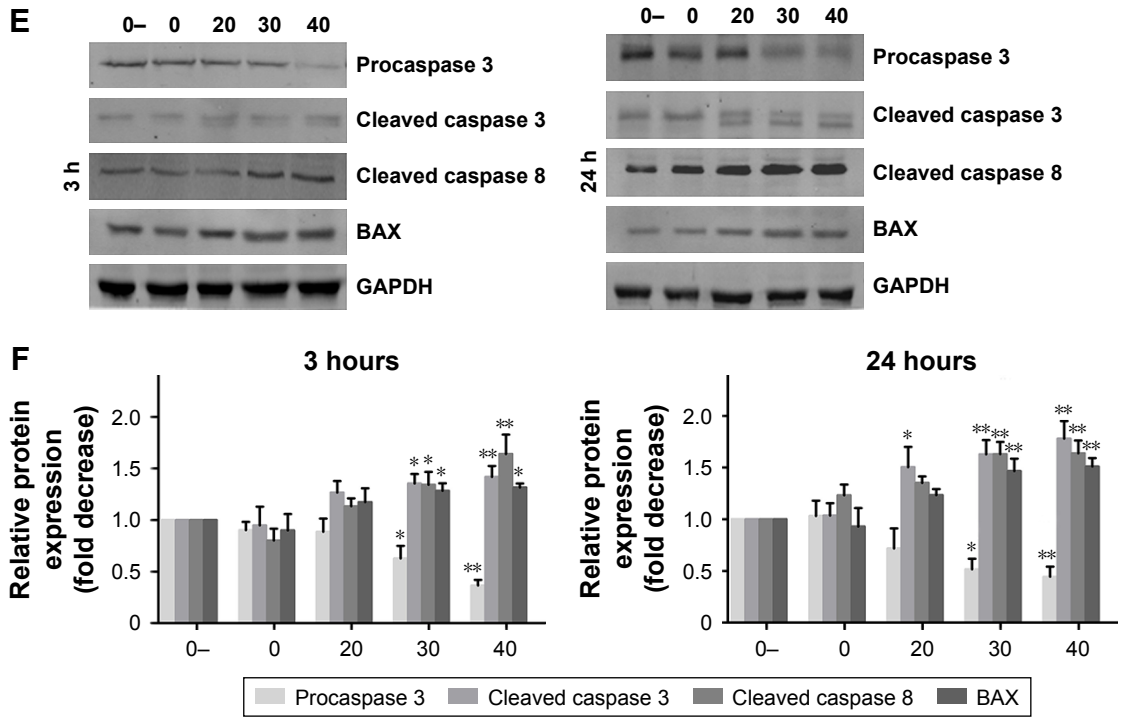

Figure 4 Au–Ag@PDA NPs induced apoptosis at 3 and 24 hours after photothermal treatment with a power density of 1 W/cm^2 for 4 minutes in T24 cells.
Notes: (**A**) Effects of Au–Ag@PDA NPs on cell apoptosis detected by FCM. (**B**) Summary of the apoptosis assay results displayed as percentages of cells in different cell death stages: necrosis, late apoptosis, early apoptosis, and live cells. (**C**) Morphological changes evaluated using Hoechst 33342 staining. (**D**) Expression levels of cell apoptosis-regulated genes detected by real-time PCR and normalized to β-actin. (**E**) Expression levels of cell apoptosis-regulated proteins determined by Western blot. GAPDH was used as the loading control. (**F**) Quantification of protein levels compared with the 0– control group (mean±SD; n=3). *P<0.05, **P<0.01, ***P<0.001 vs 0 group. (0–: 0 μg+no laser, 0: 0 μg+laser, 20: 20 μg+laser, 30: 30 μg+laser, 40: 40 μg+laser).
Abbreviations: FCM, flow cytometry; NPs, nanoparticles; PDA, polydopamine.

the mRNA expression levels of the anti-apoptosis factors BCL2 and BCLX were significantly reduced, whereas the protein expression level of the proapoptotic protein BAX was remarkably increased. Furthermore, the expression levels of specific apoptotic signal transduction molecules such as procaspase-3 were decreased, whereas cleaved caspase-3 and cleaved caspase-8 levels were increased in a time- and dose-dependent manner in the Au–Ag@PDA NPs plus laser irradiation–treated T24 cells (Figure 4E and F).

Effects of Au–Ag@PDA NPs on δΨm

Apoptosis can be initiated through one of two pathways: the extrinsic pathway by activation of cell surface death receptors and the intrinsic (mitochondrial) pathway by the release of mitochondria-related signal proteins.[26,27] To confirm the involvement of the mitochondrial pathway in the apoptosis induced by photothermal exposure of Au–Ag@PDA NPs, changes in ΔΨm were detected using the fluorescent mitochondrial probe JC-1 and then analyzed by FCM. As shown in Figure 5A, Au–Ag@PDA NPs induced a significant loss in ΔΨm after laser irradiation, as evidenced by a decrease in the red/green fluorescence intensity ratio compared to the control (Figure 5B). To evaluate the possibility that disruption of mitochondrial membrane function results in the release of cytochrome *c* from mitochondria to the cytosol, we measured the level of cytosolic cytochrome *c* by a Western blot assay. As shown in Figure 5C and D, the level of cytosolic cytochrome *c* was increased in the Au–Ag@PDA NPs plus laser irradiation group compared with that of the control group.

Au–Ag@PDA NPs induce autophagy of T24 cells

We next investigated the effect of Au–Ag@PDA NPs on autophagy as a potential antiproliferation mechanism. LC3 protein, which is an important marker of the autophagic process, forms LC3-I and LC3-II in cells. LC3-I (the LC3 precursor) is diffusely localized in the cytosol and can be converted to LC3-II (the autophagic vesicle-associated form) during formation of the autophagosome; thus, the conversion of LC3-I to LC3-II is commonly used to evaluate autophagic activity.[28] As shown in Figure 6A and B, the levels of LC3-II were increased in the T24 cells treated with different concentrations of Au–Ag@PDA NPs followed by 808 nm NIR laser irradiation, indicating that autophagy was triggered.

Another good hallmark of autophagy activation is the accumulation of LC3 punctate foci, which represents the

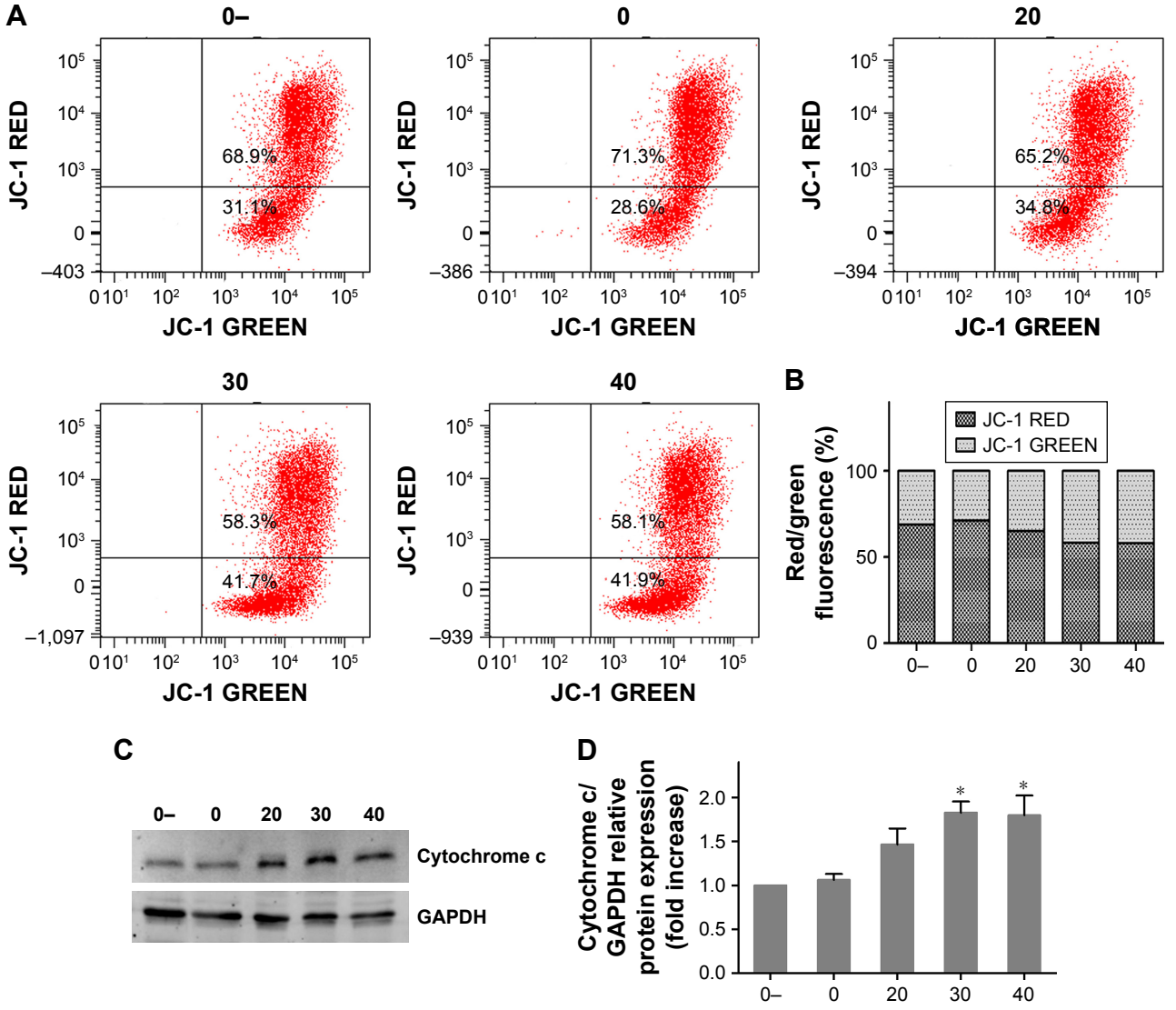

Figure 5 Changes of ΔΨm and the release of cytochrome *c* in T24 cells treated with different concentrations of Au–Ag@PDA NPs at 3 hours after laser irradiation with 1 W/cm^2 for 4 minutes.

Notes: (**A**) The ΔΨm of T24 cells was determined by FCM using JC-1 staining. (**B**) Red/green fluorescence intensity ratios. (**C**) Level of cytosolic cytochrome *c* measured by Western blot. GAPDH was used as the loading control. (0–: 0 μg+no laser, 0: 0 μg+laser, 20: 20 μg+laser, 30: 30 μg+laser, 40: 40 μg+laser). (**D**) Quantification analysis of cytochrome *c*/GAPDH compared with the 0– control group (mean±SD; n=3). *$P<0.05$ vs 0 group.

Abbreviations: ΔΨm, mitochondrial membrane potential; FCM, flow cytometry; NPs, nanoparticles; PDA, polydopamine.

recruitment of LC3-II to autophagic vacuoles.[29] Thus, to further determine that Au–Ag@PDA NPs plus laser irradiation can activate autophagy, the formation of GFP-LC3 punctate foci was investigated in the presence of Au–Ag@PDA NPs. Compared with the no Au–Ag@PDA NPs control group, large numbers of GFP-LC3 punctate foci were observed in the cytoplasm near the nucleus in HeLa cells stably expressing GFP-LC3 with Au–Ag@PDA NPs under 808 nm laser irradiation (Figure 6C). These results confirmed that Au–Ag@PDA NPs with laser irradiation could induce autophagy.

Effects of Au–Ag@PDA NPs on the AKT/ERK signaling pathway

Some studies have suggested that the AKT/ERK signaling pathway plays an important role in a wide range of cellular responses, including proliferation, apoptosis, and autophagy.[30,31] Therefore, we investigated whether the AKT/ERK signaling pathway is involved in the inhibitory effects of Au–Ag@PDA NPs, through measurement of the phosphorylated forms of AKT and ERK1/2 with Western blot analysis. As shown in Figure 7A and B, an increased Au–Ag@PDA NPs concentration followed by exposure

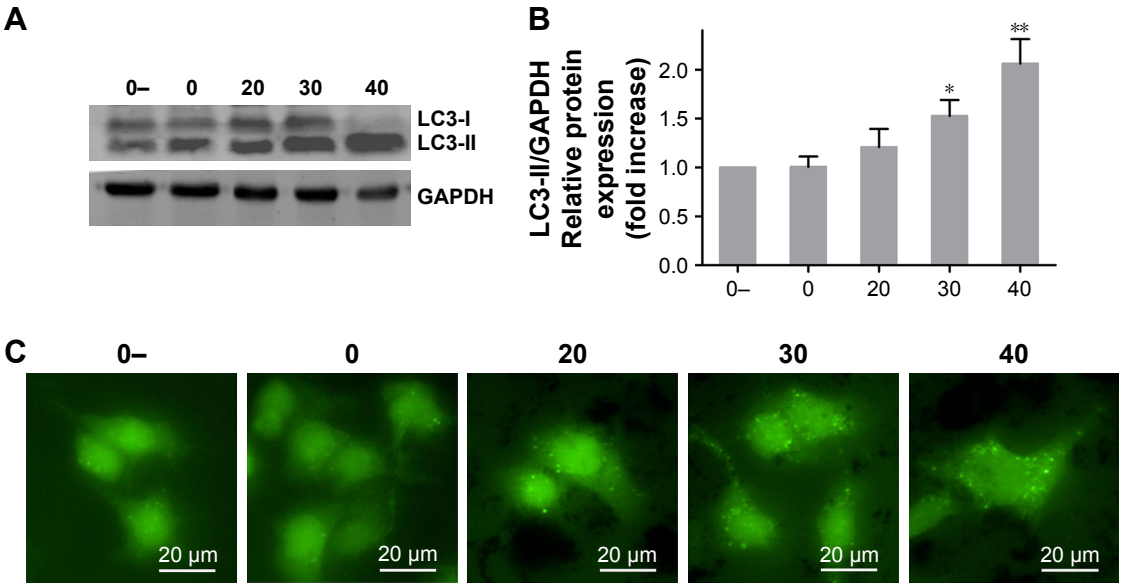

Figure 6 Au–Ag@PDA NPs triggered autophagy in cancer cells in a dose-dependent manner after being irradiated by an 808 nm laser with a power density of 1 W/cm^2 for 4 minutes.

Notes: (**A**) Expression of LC3 protein in T24 cells treated with different concentrations of Au–Ag@PDA NPs determined by Western blot analysis. (**B**) Quantification of LC3-II/GAPDH compared with the 0– control group (mean±SD; n=3). (**C**) GFP-LC3 protein and GFP-LC3 punctate foci visualized by the High-Content Imaging System in GFP-LC3 stably transfected HeLa cells treated with different concentrations of Au–Ag@PDA NPs. (0–: 0 μg+no laser, 0: 0 μg+laser, 20: 20 μg+laser, 30: 30 μg+laser, 40: 40 μg+laser). *$P<0.05$, **$P<0.01$ vs 0 group.

Abbreviations: NPs, nanoparticles; PDA, polydopamine.

to laser irradiation downregulated the phosphorylation of Ser473-AKT in a dose-dependent manner, but there were no obvious changes in the total amount of AKT. In addition, Au–Ag@PDA NPs inhibited the phosphorylation of ERK without affecting the amount of total ERK protein.

Effects of Au–Ag@PDA NPs on ROS generation

ROS generation is generally considered as one of the key mediators linked to apoptosis and autophagy.[32] FCM showed a steady concentration-dependent increase in ROS levels in the form of increased dichloro-fluorescein (DCF) fluorescence intensity in cells treated with Au–Ag@PDA NPs under laser irradiation (Figure 8A). This effect was confirmed based on direct observation of the change in fluorescence intensity under fluorescence microscopy; cells treated with Au–Ag@PDA NPs plus laser irradiation exhibited stronger fluorescence than the control cells (Figure 8B and C), which confirmed the great ability of Au–Ag@PDA NPs to promote ROS production after laser irradiation.

Au–Ag@PDA NPs inhibit tumor growth in a xenograft mouse model

To confirm the inhibitory effects of Au–Ag@PDA NPs on the growth of T24 cells in vivo, we established a xenograft mouse model. As shown in Figure 9A and B, all Au–Ag@PDA NPs plus laser irradiation-treated mice, especially those injected with high-dose NPs, exhibited dramatic suppression in tumor growth compared to that of the control group.

To evaluate the potential toxicity of Au–Ag@PDA NPs, the body weight of the nude mice was constantly monitored. The Au–Ag@PDA NPs-treated mice showed no significant loss in body weight compared with the control group (Figure 9C). In addition, histological analysis by H&E staining of the major organs showed no noticeable morphological changes in the heart, liver, spleen, lung, and kidney in both treatment groups compared with the control group after 12 days of photothermal therapy, further indicating the low toxicity of the Au–Ag@PDA NPs in vivo (Figure 9D).

To identify the mechanism of action of Au–Ag@PDA NPs in vivo, H&E and TUNEL staining of tumor tissues were performed. In the H&E assay, extensive nuclear shrinkage, fragmentation, and absence were detected in Au–Ag@PDA NPs-treated tumors exposed to laser irradiation, which may have led to significant inhibition of the tumor (Figure 9E). The TUNEL assay further supported the in vitro effects of Au–Ag@PDA NPs apoptosis induction in the transplanted T24 cell xenograft mouse model (Figure 9F).

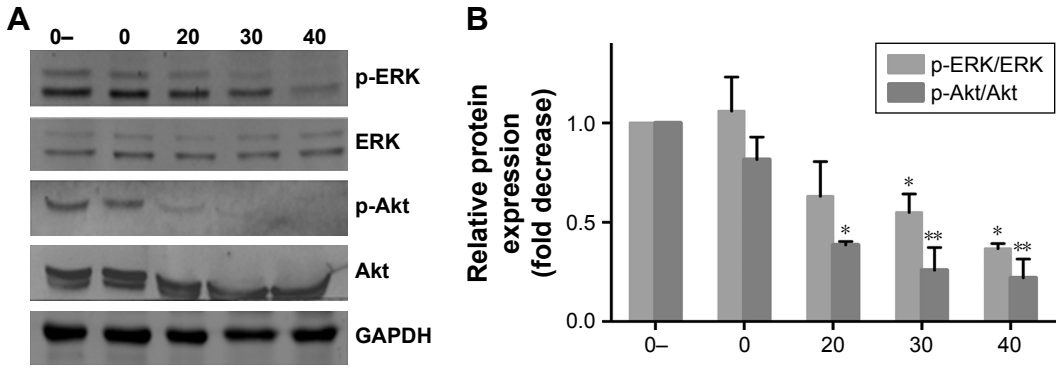

Figure 7 Changes in AKT and ERK signaling pathways in T24 cells treated with different concentrations of Au–Ag@PDA NPs after laser irradiation with 1 W/cm^2 for 4 minutes.

Notes: (**A**) Expression levels of phosphorylated AKT and ERK detected by Western blot analysis. (**B**) Quantification of p-AKT/AKT and p-ERK/ERK levels compared with the 0– control group (mean±SD; n=3). (0–: 0 μg+no laser, 0: 0 μg+laser, 20: 20 μg+laser, 30: 30 μg+laser, 40: 40 μg+laser). *P<0.05, **P<0.01 vs 0 group.

Abbreviations: NPs, nanoparticles; PDA, polydopamine.

Discussion

Photothermal therapy is an alternative effective cancer treatment, particularly for solid tumors that are resistant to other treatments. Photothermal nanomaterials are directed at tumors for several minutes, thereby killing them with localized heat. Au–Ag@PDA NPs represent a novel nanomaterial exhibiting better structural stability, biocompatibility, and higher photothermal transduction efficiency than conventional Au NPs, and also showed a more efficient inhibitory effect on the proliferation of HeLa cells, implying their potential value in cancer treatment.[18] In this study, we found that Au–Ag@PDA NPs also inhibited the proliferation of T24

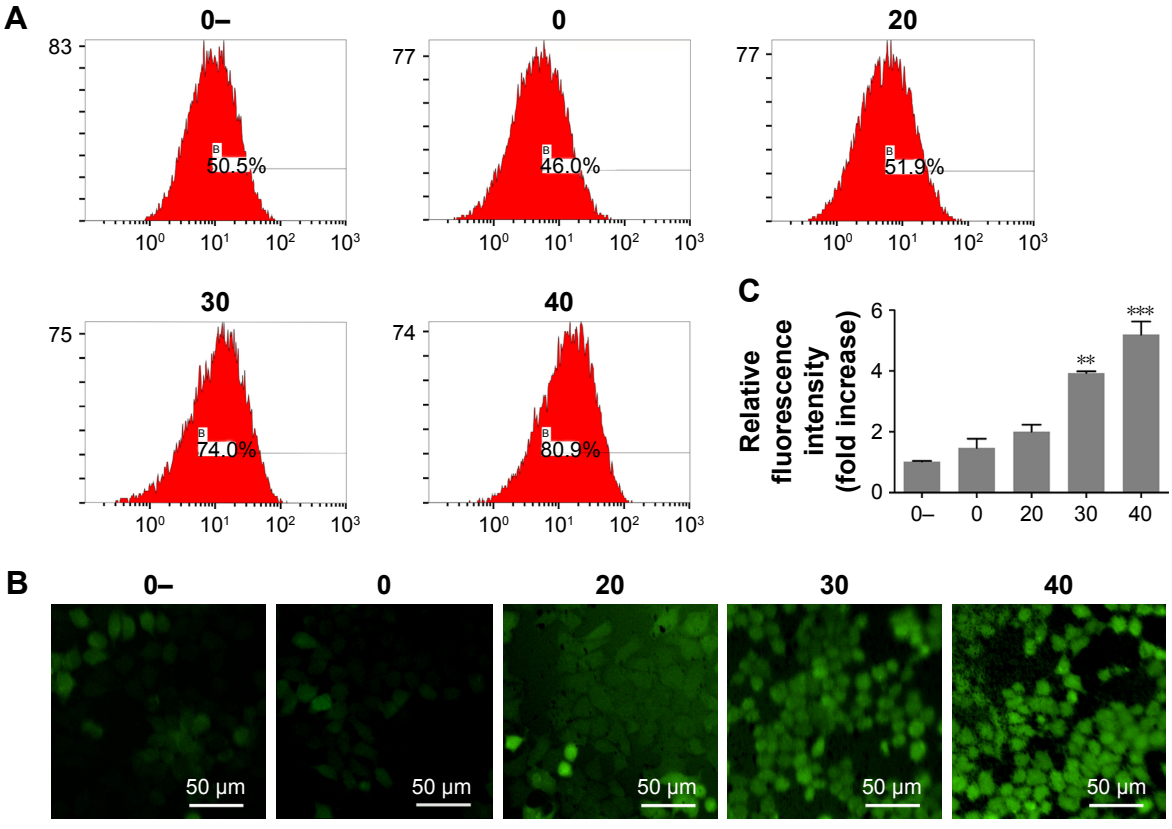

Figure 8 ROS generation in T24 cells incubated with different concentrations of Au–Ag@PDA NPs at 3 hours after photothermal treatment with a power density of 1 W/cm^2 for 4 minutes.

Notes: (**A**) ROS levels evaluated by FCM. (**B**) ROS levels observed by fluorescent microscopy. (**C**) Mean fluorescence intensity ratio compared with the 0– control group (mean±SD; n=3). (0–: 0 μg+no laser, 0: 0 μg+laser, 20: 20 μg+laser, 30: 30 μg+laser, 40: 40 μg+laser). **P<0.01, ***P<0.001 vs 0 group.

Abbreviations: FCM, flow cytometry; NPs, nanoparticles; PDA, polydopamine.

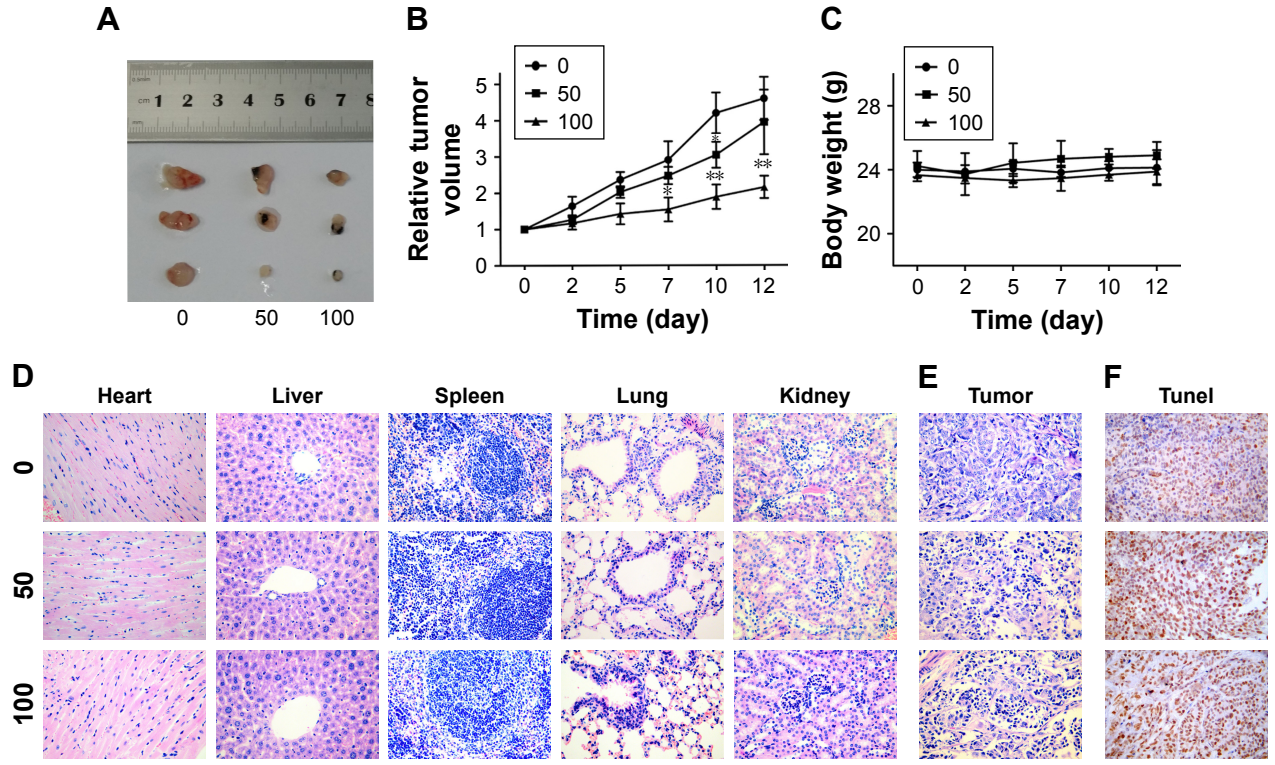

Figure 9 Au–Ag@PDA NPs suppressed tumor growth after photothermal therapy with a power density of 1 W/cm² for 4 minutes in vivo.
Notes: (**A**) Representative images of tumors isolated from nude mice at 12 days after laser irradiation. (**B**) Tumor volume at each time interval measured during treatment. (**C**) Body weights of the mice monitored during treatment. (**D**) H&E staining of the major organs isolated from different groups of nude mice at 12 days after laser irradiation. (**E**) H&E staining and (**F**) TUNEL staining of tumors from different groups of nude mice at 12 days after laser irradiation. *$P<0.05$, **$P<0.01$ vs 0 group.
Abbreviations: NPs, nanoparticles; PDA, polydopamine.

human bladder cancer cells, and further characterized the molecular mechanisms of the anticancer effect of Au–Ag@PDA NPs in vitro and in vivo, which were found to be largely mediated through inducing cell cycle S arrest, apoptosis, and autophagy.

Cell cycle deregulation is one of the major hallmarks of cancer cells; thus, the induction of cell cycle arrest may be an effective strategy to control the aberrant proliferation of cancer cells.[33] Our results demonstrated that the S phase arrest of T24 cells following Au–Ag@PDA NPs treatment with laser irradiation was associated with a decrease in the protein levels of cyclin A and an increase in the protein levels of p21. Cyclin A is present in the nucleus during the S phase, where it participates in the initiation and completion of DNA replication.[34] p21 has also been reported as a potent inhibitor of cyclin-dependent kinases capable of arresting cell cycle progression.[35] Thus, these results indicate that Au–Ag@PDA NPs plus laser irradiation may modulate the expression of cell cycle-related proteins to induce S phase arrest and consequently inhibit the proliferation of T24 cells.

Apoptosis is a cell death mechanism and can be activated by compounds targeting extrinsic and intrinsic (mitochondrial) pathways. The extrinsic pathway is related to activation of cell surface death receptors such as Fas and TNF-R. Alternatively, the mitochondria-mediated intrinsic pathway may be initiated by many stress conditions; indeed, chemotherapeutic agents and drugs have been shown to trigger the release of mitochondria-related signal proteins.[26,27] For the mitochondria-mediated intrinsic pathway, the release of cytochrome *c* from the mitochondrial membrane into the cytosol is fundamental to apoptosome formation and activation of the caspase family.[36] Members of the BCL2 family also play a significant role in apoptosis by controlling mitochondrial membrane permeability and facilitating the passage of cytochrome *c*.[37] We found that Au–Ag@PDA NPs induced an increase in BAX and a decrease in BCL2 levels, and further provoked depolarization of the $\Delta\Psi m$ and the consequent release of cytochrome *c* into the cytosol. Based on previous studies and our results, an imbalance of BAX and BCL2 proteins after treatment with Au–Ag@PDA NPs along with laser irradiation may lead to the loss of $\Delta\Psi m$, resulting in the release of cytochrome *c* from the mitochondria into the cytosol to trigger caspase-8 and caspase-3 activation, ultimately causing apoptosis in T24 cells. Nevertheless, these findings do not

rule out the possibility that activation of extrinsic pathways may also be involved in Au–Ag@PDA NPs-induced cell apoptosis, since we did not explore the effect on cell surface death receptors.

Autophagy is another antiproliferation pathway that plays an essential role in determining cellular fate. Recently, several studies demonstrated that Au NPs can induce autophagy by upregulation of autophagy proteins as well as formation of autophagosomes.[38] Our results confirm these previous findings, given that Au–Ag@PDA NPs promoted remarkable levels of autophagy activity as evidenced by the conversion of LC3-I to LC3-II and the accumulation of LC3 punctate foci. In mammalian cells, apoptosis and autophagy are regulated by several important intracellular signaling pathways, including the AKT/ERK signaling pathway.[30,31] Au–Ag@PDA NPs plus laser irradiation caused significant inhibition of AKT and ERK phosphorylation. The AKT and ERK proteins exist in a phosphorylated form and suppress apoptosis and autophagy under normal conditions; however, when the levels of phosphorylated AKT and ERK are downregulated, apoptosis and autophagy are triggered,[30,39] indicating that blockage of this pathway might underlie the Au–Ag@PDA NPs-induced excessive apoptosis and autophagy. Apoptosis and autophagy are both highly regulated biological processes that may take place independently; however, in most circumstances, both processes are tightly connected by some common upstream signaling components. Therefore, our future studies will investigate whether both processes have substantial interconnections in inducing cell death under Au–Ag@PDA NPs along with laser irradiation.

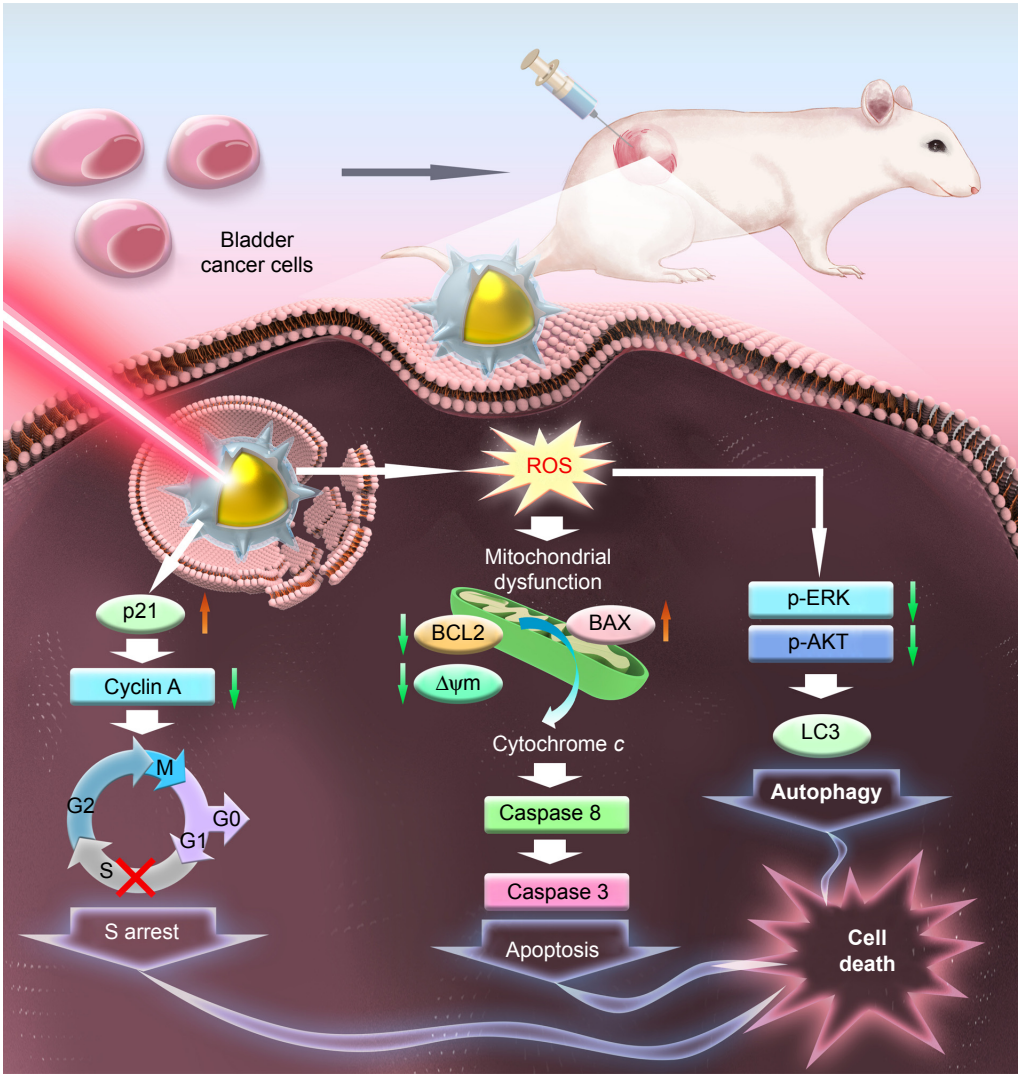

Figure 10 Possible molecular mechanisms of Au–Ag@PDA NPs as photothermal conversion materials for bladder cancer therapy.
Abbreviations: NPs, nanoparticles; PDA, polydopamine.

ROS are critical signaling molecules that regulate many signal transduction pathways, and excessive generation of ROS may interfere with cellular signaling pathways and activate subsequent apoptotic and autophagy processes. Therefore, ROS are considered one of the earliest hallmarks of these cell death processes compared to other markers.[39] For instance, ROS have been shown to lead to the induction of the intrinsic pathway of apoptosis by regulating the activity of the BCL2 family protein via two main mechanisms: direct oxidation of BCL2 leading to abrogation of its antiapoptotic activity, and decreasing the ubiquitination of BAX and increasing the ubiquitination of BCL2.[32] ROS generation has also been shown to regulate AKT/ERK activity and is subsequently associated with the classical markers of autophagy such as induction of LC3 and conversion of LC3-I to LC3-II.[30,31] Given that exposure to Au–Ag@PDA NPs after laser irradiation significantly enhanced ROS production in T24 cells, it is possible that the Au–Ag@PDA NPs-triggered apoptosis, autophagy, and block of the AKT/ERK signaling pathway are related to excessive ROS generation.

A successful anticancer treatment should efficiently inhibit the proliferation of cancer cells in vivo. Indeed, Au–Ag@PDA NPs significantly inhibited tumor growth in transplanted T24 cell xenografted mice after photothermal therapy. Although some skin burning was observed directly over the tumor surface in the high-dose Au–Ag@PDA NPs treatment groups, the skin repaired itself after about 10 days. More importantly, there was no observable in vivo toxicity in any of the Au–Ag@PDA NPs plus laser exposure treatment groups, suggesting that the biocompatibility of Au–Ag@PDA NPs is suitable for in vivo photothermal therapy.

In conclusion, Au–Ag@PDA NPs were taken up by the T24 cells through an endocytosis process, localizing mostly in the lysosomes. Au–Ag@PDA NPs exhibited low cytotoxicity, but after laser irradiation, the NPs could effectively inhibit the proliferation of T24 cells by altering the expression of cell cycle–related proteins cyclin A and p21 to cause S phase arrest, leading to cell death by inducing mitochondria-mediated cellular apoptosis and increasing LC3-II protein expression and LC3 punctate foci to trigger autophagy, accompanied by blocking the AKT/ERK signaling pathway and excessive ROS generation (Figure 10). In the xenograft mouse model, Au–Ag@PDA NP-mediated photothermolysis also showed significant antitumor activity with low levels of toxicity. These findings revealed the multiple cytotoxic mechanisms and potential clinical application of Au–Ag@PDA NPs in the treatment of bladder cancer.

Acknowledgments

This study was supported by grants from the National Natural Science Foundation of China (Nos 31401086, 81402338, 81402395, and 81703034), Jilin Province Science and Technology Development Program (No 20150520157JH), the China Postdoctoral Science Foundation Grant (No 2015M581398), and the Bethune program of Jilin University (No 2015309). This work was also supported by the Jilin Provincial Health Project (Nos sczsy201614 and sczsy201716) and Jilin Province Health Service Capacity Improvement Project (No 2017F014).

Disclosure

The authors report no conflicts of interest in this work.

References

1. Zhang CL, Lv KP, Cong HP, Yu SH, Kp L, Sh Y. Controlled assemblies of gold nanorods in PVA nanofiber matrix as flexible free-standing SERS substrates by electrospinning. *Small*. 2012;8(5):648–653.
2. Tian G, Zhang X, Gu Z, Zhao Y. Recent advances in upconversion nanoparticles-based multifunctional nanocomposites for combined cancer therapy. *Adv Mater*. 2015;27(47):7692–7712.
3. Liu J, Zheng X, Yan L, et al. Bismuth sulfide nanorods as a precision nanomedicine for in vivo multimodal imaging-guided photothermal therapy of tumor. *ACS Nano*. 2015;9(1):696–707.
4. Tong L, Zhao Y, Huff TB, Hansen MN, Wei A, Cheng JX. Gold nanorods mediate tumor cell death by compromising membrane integrity. *Adv Mater*. 2007;19:3136–3141.
5. Norman RS, Stone JW, Gole A, Murphy CJ, Sabo-Attwood TL. Targeted photothermal lysis of the pathogenic bacteria, *Pseudomonas aeruginosa*, with gold nanorods. *Nano Lett*. 2008;8(1):302–306.
6. Shi J, Wang L, Zhang J, et al. A tumor-targeting near-infrared laser-triggered drug delivery system based on GO@Ag nanoparticles for chemo-photothermal therapy and X-ray imaging. *Biomaterials*. 2014;35(22):5847–5861.
7. Guo F, Yu M, Wang J, Tan F, Li N. Smart IR780 theranostic nanocarrier for tumor-specific therapy: hyperthermia-mediated bubble-generating and folate-targeted liposomes. *ACS Appl Mater Interfaces*. 2015;7(37):20556–20567.
8. Sheng W, He S, Seare WJ, Almutairi A. Review of the progress toward achieving heat confinement – the holy grail of photothermal therapy. *J Biomed Opt*. 2017;22(8):80901.
9. Ungureanu C, Kroes R, Petersen W, et al. Light interactions with gold nanorods and cells: implications for photothermal nanotherapeutics. *Nano Lett*. 2011;11(5):1887–1894.
10. Tong L, Wei Q, Wei A, Cheng JX. Gold nanorods as contrast agents for biological imaging: optical properties, surface conjugation and photothermal effects. *Photochem Photobiol*. 2009;85(1):21–32.
11. Huang X, Jain PK, El-Sayed IH, El-Sayed MA. Gold nanoparticles: interesting optical properties and recent applications in cancer diagnostics and therapy. *Nanomedicine*. 2007;2(5):681–693.
12. Wang C, Bao C, Liang S, et al. RGD-conjugated silica-coated gold nanorods on the surface of carbon nanotubes for targeted photoacoustic imaging of gastric cancer. *Nanoscale Res Lett*. 2014;9(1):264.
13. Liu Y, Yang M, Zhang J, et al. Human induced pluripotent stem cells for tumor targeted delivery of gold nanorods and enhanced photothermal therapy. *ACS Nano*. 2016;10(2):2375–2385.
14. Zhang Z, Wang L, Wang J, et al. Mesoporous silica-coated gold nanorods as a light-mediated multifunctional theranostic platform for cancer treatment. *Adv Mater*. 2012;24(11):1418–1423.

15. Mehtala JG, Torregrosa-Allen S, Elzey BD, et al. Synergistic effects of cisplatin chemotherapy and gold nanorod-mediated hyperthermia on ovarian cancer cells and tumors. *Nanomedicine*. 2014;9(13):1939–1955.
16. Huang P, Xu C, Lin J, et al. Folic acid-conjugated graphene oxide loaded with photosensitizers for targeting photodynamic therapy. *Theranostics*. 2011;1:240–250.
17. Liang S, Li C, Zhang C, et al. CD44v6 monoclonal antibody-conjugated gold nanostars for targeted photoacoustic imaging and plasmonic photothermal therapy of gastric cancer stem-like cells. *Theranostics*. 2015; 5(9):970–984.
18. Ataee-Esfahani H, Wang L, Nemoto Y, Yamauchi Y. Synthesis of bimetallic Au@Pt nanoparticles with Au core and nanostructured Pt shell toward highly active electrocatalysts. *Chem Mater*. 2010;22(23): 6310–6318.
19. Wang L, Yamauchi Y. Strategic synthesis of trimetallic Au@Pd@Pt core–shell nanoparticles from poly(vinylpyrrolidone)-based aqueous solution toward highly active electrocatalysts. *Chem Mater*. 2011;23(9): 2457–2465.
20. Wang H, Jeong HY, Imura M, et al. Shape- and size-controlled synthesis in hard templates: sophisticated chemical reduction for mesoporous monocrystalline platinum nanoparticles. *J Am Chem Soc*. 2011;133(37): 14526–14529.
21. Li C, Sato T, Yamauchi Y. Electrochemical synthesis of one-dimensional mesoporous Pt nanorods using the assembly of surfactant micelles in confined space. *Angew Chem Int Ed Engl*. 2013;52(31):8050–8053.
22. Jiang B, Li C, Malgras V, Imura M, Tominaka S, Yamauchi Y. Mesoporous Pt nanospheres with designed pore surface as highly active electrocatalyst. *Chem Sci*. 2016;7(2):1575–1581.
23. Li J, Wang W, Zhao L, et al. Hydroquinone-assisted synthesis of branched Au–Ag nanoparticles with polydopamine coating as highly efficient photothermal agents. *ACS Appl Mater Interfaces*. 2015;7(21): 11613–11623.
24. Roper DK, Ahn W, Hoepfner M. Microscale heat transfer transduced by surface plasmon resonant gold nanoparticles. *J Phys Chem C Nanomater Interfaces*. 2007;111(9):3636–3641.
25. Tian Q, Jiang F, Zou R, et al. Hydrophilic Cu9S5 nanocrystals: a photothermal agent with a 25.7% heat conversion efficiency for photothermal ablation of cancer cells in vivo. *ACS Nano*. 2011;5(12):9761–9771.
26. Razaghi A, Heimann K, Schaeffer PM, Gibson SB. Negative regulators of cell death pathways in cancer: perspective on biomarkers and targeted therapies. *Apoptosis*. 2018;23(2):93–112.
27. Ke B, Tian M, Li J, Liu B, He G. Targeting programmed cell death using small-molecule compounds to improve potential cancer therapy. *Med Res Rev*. 2016;36(6):983–1035.
28. Karim MR, Kanazawa T, Daigaku Y, et al. Cytosolic LC3 ratio as a sensitive index of macroautophagy in isolated rat hepatocytes and H4-II-E cells. *Autophagy*. 2007;3(6):553–560.
29. Razi M, Chan EY, Tooze SA. Early endosomes and endosomal coatomer are required for autophagy. *J Cell Biol*. 2009;185(2):305–321.
30. Cagnol S, Chambard JC. ERK and cell death: mechanisms of ERK-induced cell death – apoptosis, autophagy and senescence. *FEBS J*. 2010;277(1):2–21.
31. Zhao GX, Pan H, Ouyang DY, He XH, Xh H. The critical molecular interconnections in regulating apoptosis and autophagy. *Ann Med*. 2015; 47(4):305–315.
32. Galadari S, Rahman A, Pallichankandy S, Thayyullathil F. Reactive oxygen species and cancer paradox: to promote or to suppress? *Free Radic Biol Med*. 2017;104:144–164.
33. Novák B, Tyson JJ. Modelling the controls of the eukaryotic cell cycle. *Biochem Soc Trans*. 2003;31(Pt 6):1526–1529.
34. Pagano M, Pepperkok R, Verde F, Ansorge W, Draetta G. Cyclin A is required at two points in the human cell cycle. *EMBO J*. 1992;11(3): 961–971.
35. Vermeulen K, Van Bockstaele DR, Berneman ZN. The cell cycle: a review of regulation, deregulation and therapeutic targets in cancer. *Cell Prolif*. 2003;36(3):131–149.
36. Kroemer G, Galluzzi L, Brenner C. Mitochondrial membrane permeabilization in cell death. *Physiol Rev*. 2007;87(1):99–163.
37. Sivakumar D, Sivaraman T. A review on structures and functions of Bcl-2 family proteins from *Homo sapiens*. *Protein Pept Lett*. 2016;23(10): 932–941.
38. Li S, Zhang C, Cao W, et al. Anchoring effects of surface chemistry on gold nanorods: modulates autophagy. *J Mater Chem B*. 2015;3(16): 3324–3330.
39. Kaminskyy VO, Zhivotovsky B. Free radicals in cross talk between autophagy and apoptosis. *Antioxid Redox Signal*. 2014;21(1):86–102.